# Natural gas potential of Carboniferous and Permian transitional shales in central Hunan, South China

Zhao, Zhenghui; Tan, Jianqiang ; Ju, Yiwen; Hilton, Jason; Yang, Rongfeng; Zhou, Ping; Huang, Yanran; Ning, Bowen; Liu, Jisong

*DOI:*
10.1016/j.jngse.2018.05.024



*Document Version*
Peer reviewed version

*Citation for published version (Harvard):*
Zhao, Z, Tan, J, Ju, Y, Hilton, J, Yang, R, Zhou, P, Huang, Y, Ning, B & Liu, J 2018, 'Natural gas potential of Carboniferous and Permian transitional shales in central Hunan, South China', *Journal of Natural Gas Science and Engineering*, vol. 55, pp. 520-533. https://doi.org/10.1016/j.jngse.2018.05.024

# Accepted Manuscript

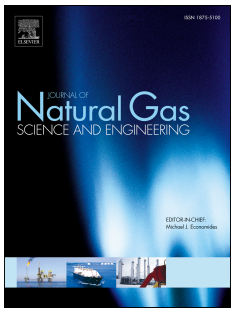


Natural gas potential of Carboniferous and Permian transitional shales in central Hunan, South China

Zhenghui Xiao, Jingqiang Tan, Yiwen Ju, Jason Hilton, Rongfeng Yang, Ping Zhou, Yanran Huang, Bowen Ning, Jisong Liu

PII: S1875-5100(18)30224-5

DOI: 10.1016/j.jngse.2018.05.024

Reference: JNGSE 2582

To appear in: *Journal of Natural Gas Science and Engineering*

Received Date: 29 July 2017

Revised Date: 22 April 2018

Accepted Date: 16 May 2018

Please cite this article as: Xiao, Z., Tan, J., Ju, Y., Hilton, J., Yang, R., Zhou, P., Huang, Y., Ning, B., Liu, J., Natural gas potential of Carboniferous and Permian transitional shales in central Hunan, South China, *Journal of Natural Gas Science & Engineering* (2018), doi: 10.1016/j.jngse.2018.05.024.

# Natural gas potential of Carboniferous and Permian transitional shales in central Hunan, South China

Zhenghui Xiao[a], Jingqiang Tan[b,*], Yiwen Ju[c], Jason Hilton[d], Rongfeng Yang[a], Ping Zhou[e], Yanran Huang[a], Bowen Ning[f], Jisong Liu[a]

[a] Hunan Key Laboratory of Shale Gas Resource Utilization, School of Resource, Environment and Safety Engineering, Hunan University of Science and Technology, Xiangtan 411201, Hunan, China

[b] Key Laboratory of Metallogenic Prediction of Nonferrous Metals and Geological Environment Monitoring, Ministry of Education, School of Geosciences and Info-Physics, Central South University, Changsha 410083, China

[c] College of Earth Sciences, University of Chinese Academy of Sciences, Beijing 100049, China

[d] School of Geography, Earth and Environmental Science, University of Birmingham, Edgbaston, Birmingham, B15 2TT, UK

[e] School of Economics, Hunan Institute of Engineering, Xiangtan 411104, Hunan, China

[f] Henan Geological Exploration Institute of China Chemical Geology and Mine Bureau, Zhengzhou 450011, Henan, China

[*] Corresponding authors: tanjingqiang@aliyun.com

## Abstract

The Carboniferous Ceshui formation and Permian Longtan and Dalong formations were deposited in transitional settings preserved in what is now central Hunan Province, South China, as they are potential natural gas plays. In this study, we analysed the total organic carbon (TOC), vitrinite reflectance (Ro), kerogen type, mineralogy, porosity, permeability, and methane adsorption of representative shale samples from these rock units. Our results indicate that TOC content can be as high as 9.2%, with a mean ($\bar{x}$) of 3.5%. The Permian shale formations were deposited in more strongly reducing environments than the

Carboniferous Ceshui shale. The kerogen composition of the Carboniferous Ceshui shale is dominated by Type III, while both of the Permian shales contain primarily Type II kerogens; Ro values range from 1.1% to 2.4% ($\bar{x}$=1.6%). The organic matter in all the studied shales is in the wet gas window of thermal maturity and is relatively less mature than Lower Palaeozoic marine shales in south China. Mineral compositions are dominated by quartz ($\bar{x}$=53.8%) and clay ($\bar{x}$=35.6%), suggesting a high brittleness index. Porosity ranges from 0.5% to 14% ($\bar{x}$=6.4%), while permeability varies from 0.0026 micro Darcy (mD) to 0.0640 mD ($\bar{x}$=0.0130 mD). The gas adsorption capacity varies from 1.24 to 4.53 $cm^3/g$ ($\bar{x}$=2.40 $cm^3/g$). Relatively less mature shale samples (Ro<1.5%) have low methane adsorption capacities, regardless of their TOC values. However, the methane adsorption capacity of more mature (Ro>1.5%) shales samples exhibit a positive correlation with TOC content.

**Keywords:** Lower Carboniferous; Upper Permian; Natural gas; Transitional shale; Unconventional reservoir; Hunan Province.

## 1. Introduction

The remarkable success of shale gas development in North America has triggered a flourishing of shale gas exploration and increased the number of investigations into the gas potential of shales worldwide (e.g., Bowker, 2007; Jarvie et al., 2007; Tang et al., 2014; Tan et al., 2015). To enhance domestic energy supply via shale gas exploitation, the Chinese government has already set ambitious plans. Geological surveys and exploration activities are underway across the country (Tan et al., 2013). To date, China has begun developing several shale gas fields in the Sichuan Basin (e.g., the Fuling, Weiyuan, and Changning shale gas blocks).

In China, three types of organic rich shale are widely distributed in sedimentary basins, comprising marine shales, marine-lacustrine transitional shales (hereafter referred to

as “transitional shales”), and lacustrine shales (Bu et al., 2015; Tan et al., 2015). Marine shales in the Cambrian and Silurian starta and transitional shales in the Carboniferous and Permian strata are widely distributed cross South China (e.g. Tan et al., 2015; Zou et al., 2010). Although natural gas has been successfully produced from the marine shales, transitional shales have not been yet successfully developed (Dong et al., 2016). In the central part of Hunan, Carboniferous and Permian transitional shales occur in thick and laterally extensive beds (Bao et al., 2016; Gu et al., 2015; Jing et al., 2013; Xu et al., 2015). Previous studies have shown that Carboniferous and Permian paralic coal-bearing strata constitute source rocks for conventional petroleum fields in this region (Wang et al., 2010; Zhan et al., 2006; Zhou et., 2014; Zhu et al., 2012). These transitional shales have been more recently identified as promising targets of shale gas exploration (Bao et al., 2016; Gu et al., 2015; Liang et al., 2014; Luo et al., 2012). National petroleum companies, including Sinopec, have already shown strong interest in developing natural gas resources from transitional shale intervals. Therefore, there is an urgent need to characterise these shale intervals and evaluate their reservoir potential.

It has been recognized that no two shale gas systems are exactly alike, and thus exploitation strategies differ from one system to the next (Tan, et al., 2015). However, prolific shale plays are commonly distinguished using certain minimal technical thresholds. These include, but are not limited to: shale lateral extent and effective thickness, organic matter richness, thermal maturity, mineralogy, porosity, permeability, adsorptive capacity, and gas-in-place (GIP) ( Bowker, 2007; Jarvie et al., 2007; Tan, et al., 2013; 2015). These indices have been widely applied to evaluate the reservoir potential of marine shales in South China. However, for transitional shales, numerous issues remain concerning the composition and source(s) of organic material, depositional environment, thermal maturity, petrophysical properties, and methane adsorption capacity. Additionally, the correlations among organic

materials, mineralogy, and depositional conditions, as well as the influences of porosity and permeability, and the relative effects of total organic carbon (TOC) and thermal maturity on methane adsorption have not been clarified. This study aims to investigate these problems through a systematic characterization of transitional shales from the Carboniferous Ceshui formation and the Permian Longtan and Dalong formations in the central region of Hunan. We comprehensively analysed the TOC content, organic matter type, thermal maturity, mineral composition, reservoir physical properties, and gas adsorption capacity of the shales. We then compared our results with those reported for prolific shale plays in China and the United States. Lastly, we discuss the correlations among the selected reservoir characterisation parameters.

## 2. Materials and Methods

### *2.1 Geological setting and shale deposition in central Hunan*

The study area is located in the Middle Yangtze Region and in the north of the South China fold system (Fig. 1a). It lies east of the Hengshan Uplift, and west of the Xuefeng Uplift. This region is tectonically composed of five subunits. From north to south they are the Lianyuan Depression, Longshan Uplift, Shaoyang Depression, Guandimiao Uplift, and the Lingling Depression (Fig. 1b). Regional faults extend primarily in the NE-NNE direction, and include the Chengbu-Xinhua fault, Qiyang Arc fault, Miluo-Shaoyang fault, Xinshao-Xinning fault, and Zhuzhou-Shuangpai fault (Fig. 2). Additionally, thrust nappe and gravity gliding structures have been formed by multiple tectonic events. The Lianyuan and Shaoyang depression began forming during the Ordovician at the onset of the Caledonian orogeny. The Qiyang arc was dominantly formed through structural deformation caused by the Triassic Indosinian orogeny (Li, et al., 2013; Wang et al., 2010).

Shales are well developed in certain formations of the study area. Sedimentary strata are characterized by carbonates interbedded with clastics deposited in the Late Palaeozoic to Middle Triassic. The region has experienced four primary sedimentary cycles from the Devonian to the Permian (Jing et al., 2013; Xu et al., 2015). The first sedimentary cycle occurred between the Tiaomajian and Qiziqiao periods during the Devonian when a transgression initiated during a large-scale geological extension and was followed by a regression generated by the Liujiang orogeny. This cycle resulted in the deposition of the Shetianqiao and Qiziqiao marine shales. The second transgression started in the Mississippian (early Carboniferous), but ended as a full-scale regression in the mid-Mississippian with the deposition of the Ceshui formation as transitional beds formed under the alternating influences of shallow marine and shoreline environments (Fig. 1c) (Shao et al., 1992). The third cycle was primarily controlled by the Dongwu tectonic movement and is the largest transgression that occurred during the development of the mid- to late Carboniferous paraplatform. However, this transgression was terminated by a full-scale regression during the early Lopingian (late Permian) (Fig. 1c), and coastal marsh shales were subsequently deposited (Gu et al., 2015; Ji et al., 2011). The fourth cycle persisted for a shorter time (i.e., only during the Lopingian), and resulted in the deposition of the Dalong formation (Fig. 1c). During this time, siliciclastic rocks, siliceous limestone, and shales were deposited in littoral-bathyal-abyssal facies (Fig. 1c) (Feng et al., 1993).

*2.2 Samples*

Fresh transitional shale samples are exposed in some outcrops of the study area. A total of 96 representative samples were collected from the Shimingqiao (SMQ), Qixingjie (QXJ), Duanpoqiao (DPQ), Tantou (TT), Doulishan (DLS), Nantang (NT), Jilong (JL), Jingzhushan (JZS), Zhaoyang (ZY), Liangshuijing (LSJ), Xiandong (XD), Lumaojiang

(LMJ), and Douling (DL) sections (Fig. 1b). Generally, shale samples were collected from at least 1 m deep, and every 10 m from the bottom to top of the exposed sections.

*2.3 Methods*

The selected samples were analysed for TOC, vitrinite reflectance (Ro), kerogen type, mineralogy, porosity, permeability, and methane adsorption.

TOC contents were measured using a Leco carbon-sulphur analyser and reported as the weight percentage (wt%) of the total rock material. Samples were crushed into a powder <200 mesh, and 1-2 g samples were pyrolysed to 600°C. Thin-sections of 42 samples were prepared for investigation mineral components and structural fabrics. The samples were examined using a Zeiss Axiophot Electronic Microscope equipped with a Carl Zeiss Axiocam digital camera and Axiovision 2.0 software. This system was capable of taking high-resolution photomicrographs under magnification of 10x, 20x, 30x, 40x, and 50x. Kerogen type was analysed by transmitted light microscopy. Thermal maturity, represented by Ro, was determined using a MVP-3 microscope photomultiplier.

A total of 25 samples were analysed with a D/max-2600 X-ray diffractometer (XRD) to quantify the principal mineralogical constituents. The diffraction data were recorded from 4° to 75° 2$\theta$ with a step width of 0.02°, and a counting time of 4 s per step. Experimental conditions were set to 40 kV and 30 mA. The measured data were analysed qualitatively using EVA (Bruker) software, and quantitatively using AutoQuant software.

High-resolution scanning electron microscopy (SEM) analysis was performed on representative samples with different TOC contents and lithological types. Small subsamples 0.3-0.5 cm thick, 0.5-1.0 cm wide, and >2 cm long were cut and prepared. The subsamples were dried in an oven at 40°C for 24 h to remove moisture. Analysis was conducted using a TESCAN VEGA scanning probe microscope, and images were obtained under high vacuum at 20 kV acceleration voltage.

Porosity was measured with an ULTRAPORE-200A helium porosimetre. Permeability was tested using an ULTRA-PERMTM200 permeametre. Measurements were performed at room temperature and normal pressure (~23°C, 102 kPa) and 50% humidity.

Methane adsorption isotherms were measured for selected moisture-equilibrated samples at 40°C. The experimental procedure was: 1) de-gas the sample, 2) conduct leak tests, 3) determine the void volume as well as the sample volume using helium expansion, 4) evacuate for 60 min at 1 MPa to remove helium, and 5) perform the methane adsorption measurement (Tan, et al., 2014a). The Langmuir isotherm was applied to model gas adsorption capacity. The equation used is: $V=V_LP/(P_L+P)$ (Pan, et al., 2015, and references therein), where $V$ is the volume of absorbed gas, $V_L$ is the Langmuir volume (on the basis of monolayer adsorption), which is the maximum adsorption capacity of the absorbent, $P$ is the gas pressure, and $P_L$ is the Langmuir pressure, at which the absorbed gas content ($V$) is equal to half of the Langmuir volume (i.e., 0.5 $V_L$).

## 3. Results

### *3.1 Organic geochemical characterization*

The TOC content of the 96 shale samples ranges from 0.4% to 9.2% (Table 1), with a mean value of 3.5%. Most of sections exhibit mean TOC contents >2%, indicating that these Carboniferous-Permian transitional shales are typically organic-rich. As shown in Tables 1 and 2, the TOC content of samples from different sections varies significantly. In general, the TOC content decreases from the Longtan shale to the Dalong shale, and again in the Ceshui shale.

Organics of the shales from the Carboniferous Ceshui formation are principally composed of vitrinite (i.e., euvitrinite and vitrodetrinite). This suggests that the organic matter is more derived from higher plants, and the organic matter constituents are

characteristic of type III kerogen (Definition can be seen in Appendix 1). In contrast, the kerogen type of the shales from the Permian Longtan and Dalong formations are dominated by exinite (i.e., abundant humic amorphous bodies and a small number of sporopollen bodies). The vitrinite (i.e. euvitrinite and vitrodetrinite) content is less than 30%. This implies that the organics of the Upper Permian shales are primarily type II kerogen (Definition can be seen in Appendix 2).

Ro values range from 1.1% to 2.4% ($\bar{x}$=1.6%) (Tables 1 and 2). This suggests that the Carboniferous-Permian transitional shales have entered into a stage of high maturation. Organic matter is located in the late wet gas and dry gas window of thermal maturity. Comparatively, Ro values are high in the Ceshui shale, and gradually reduce from these samples to the Longtan shale, and finally the Dalong shale, reflecting a burial depth control on thermal maturity.

### *3.2 Mineralogy and lithology*

#### 3.2.1 Mineralogy

The XRD mineralogical data are shown in Table 2. Major constituents are quartz and clay minerals. Minor mineral components include calcite, feldspar, and pyrite. The quartz content ranges between 39.0% and 86.2% ($\bar{x}$=53.8%) and clay minerals range from 11.0% to 69.1% ($\bar{x}$=35.6%). Interestingly, the total amount of brittle minerals (i.e., quartz, feldspar, calcite, and dolomite) is >60% (Table 2), indicating that the condition of the shale is likely favourable for the application of hydraulic fracturing.

As shown in Fig. 3 and Table 2, mineralogical composition varies among shale intervals. Some of the Permian Dalong shale samples are characterized by higher contents of quartz and calcite and have lower clay mineral contents than average. The pyrite content of most of the samples is generally below the detection level of XRD technology. Nevertheless,

some of the Longtan shale samples and others from the Dalong formation exhibit much higher pyrite concentrations that can exceed 10%. Additionally, the clay mineral content of the Ceshui shale samples is generally higher than that from the other two shale intervals.

3.2.2 Lithology

Based on XRD analysis (Table 2) as well as the structural fabrics identified by thin-section examination (Fig. 4), five primary lithological facies can be distinguished for the shale samples investigated: 1) non-laminated shale, 2) carbonaceous shale, 3) calcareous shale, 4) silty shale, and 5) siliceous shale.

Non-laminated shale (Figs. 4b and c) is the most common lithofacies type. Quartz and clay minerals are predominant components, while feldspar and pyrite are relatively rare. The TOC content of non-laminated shale is highly variable, ranging from <1% to >6%.

Carbonaceous shale (Figs. 4d and e) is less common than non-laminated shale but is the second most abundant lithofacies type except in the Dalong formation. This lithofacies is dark-coloured and has a high TOC content that is generally >6% (Table 2). The sediments are poorly laminated, and the primary constituents are quartz, clay, pyrite, and organic matter.

Calcareous shale is one of the more common lithofacies in shales from the Dalong and Ceshui formations, but it is relatively rare in the Longtan formation (Table 2 and Fig. 4a). The sediments of this lithofacies are typically faintly- to well-laminated depending upon the orientation of the interbedded quartz and organic matter (Fig. 4a). The calcite content in calcareous shale samples accounts for about 30-50%, while TOC content is highly variable, and ranges from <1% to >4% (Table 2).

The silty shale is greyish black. It is mainly composed of clay minerals, and a small amount of quartz and feldspar. The TOC content is generally <1%.

The siliceous shale is dark-coloured and very hard, and primarily occurs in the Dalong formation. Siliceous shale is characterized by a high quartz content (>85%, Table 2), and the TOC content is commonly higher than that of silty and calcareous shales (Table 2).

### *3.3 Petrophysical properties*

#### 3.3.1 Reservoir storage space

SEM analysis was performed on the selected samples to characterize pores and fractures. Organic matter pores, interparticle pores (between grains), intraparticle pores (within mineral grains), and microfractures are all present in the samples (Fig. 5). Organic matter pores (Fig. 5a and b) are well-developed in most of the samples, particularly in high TOC shales. Interparticle pores (Fig. 5b, d and f) can be seen around and between crystals of quartz and feldspar or located within the clay crystals. Intraparticle pores (Figs. 5b–d) primarily occur inside pyrite framboids, and in carbonate- and feldspar-rich samples. Strip-like microfractures often can be seen between clay crystal, or between clay laminae and silty laminae (Figs. 5a, d–e).

#### 3.3.2 Porosity and Permeability

The results of porosity and permeability analyses are listed in Table 3. Porosity ranges from 0.5% to 14.0% ($\bar{x}$=6.4%) and permeability ranges from 0.0026 micro Darcy (mD) to 0.0640 mD ($\bar{x}$=0.0130 mD). Shales from the Longtan formation generally have a higher porosity and permeability than samples from the Dalong and Ceshui formations.

### *3.4 Gas Adsorption Capacity*

The high-pressure methane adsorption capacities (i.e., the maximum adsorbed gas amount) for the moisture-equilibrated shale samples vary from 1.24 $cm^3/g$ to 4.53 $cm^3/g$ ($\bar{x}$=2.40 $cm^3/g$) (Fig. 6), indicating a strong methane adsorptive potential.

## 4. Discussion

### *4.1 Organic matter in the shale*

TOC represents the richness of organic matter in source rocks. Promising conventional or unconventional source rocks generally have high TOC concentrations (Jarvie et al., 2007). Previous studies have suggested that high pyrite content in shales represents strongly reducing environmental conditions that are favourable for the enrichment and preservation of organic matter (Liang et al., 2014; Tan et al., 2014b, 2015; Wu et al., 2014). As shown in Table 2, shales with high pyrite contents tend to have high TOC contents as well. Given the relatively high TOC contents of the shale samples studied here, this suggests that the analysed transitional shales were most likely deposited in strongly reducing conditions. In fact, transitional sedimentary environments in the study area were dominated by stable and anoxic conditions through the depositional period of the shales (Dang et al., 2016; Liang et al., 2014; Tang et al., 2016). Because the Longtan shale normally exhibits higher TOC and pyrite contents, this formation may have been deposited in more strongly reducing environments compared to shales from the Dalong and Ceshui formations. However, the higher TOC concentration may also indicate a better and/or stronger organic input. According to the results of kerogen typing, the organic matter of the Ceshui shale is dominated by type III kerogen, whereas >70% of the macerals from the Permian shale are type II organics. This suggests that most of the organics found in the Permian shales are derived from marine plankton (i.e., marine microflora and microfauna). However, it has previously been documented that more derived, terrestrial plants were extensively distributed in and near the littoral swamps in this part of China during both the Mississippian and Lopingian (e.g., Ji et al., 2011; Shao et al., 1992). While this suggests that the organic input from terrestrial plants for both the Carboniferous and Permian shales should generally be similar, the observed

organic matter in the Permian shale includes much more marine plankton than the Carboniferous shale.

### *4.2 Favourable geological conditions for natural gas accumulation in shales*

#### 4.2.1 Organic geochemistry

High TOC content generally suggests that conventional and unconventional petroleum resources are promising for exploration and exploitation (Dang et al., 2016; Jarvie et al., 2007; Tan et al., 2015). TOC values significantly vary among shale reservoirs, but the productive shale gas plays normally exhibit TOC contents >2% (Tan, et al., 2015). Li et al. (2015) reported that the TOC content of the Longtan shale in South China ranges from 0.4% to 14.6%, with a mean of 4.5%. Gu et al. (2015) and Bao et al. (2016) also documented that more than half of analysed Permian shale samples exhibit TOC contents >2%. Compared to productive shale gas plays in the United States, such as the Barnett shale (Dong et al., 2016), and the transitional shales in the Bohai Bay basin and Southern North China basin (Dang et al., 2016; He et al., 2016;), TOC contents of the transitional shales in the study area are even higher. This indicates that the transitional shales in central Hunan have excellent initial potential for petroleum generation.

The organic matter type of current exploration targets for shale gas is primarily dominated by type II kerogen (e.g., the Barnett, Marcellus, and Haynesville shale plays in the United States; the shale gas formations in the Western Canadian basin; and the Longmaxi shale in South China) (Dong et al., 2016) (Table 4). Nevertheless, thick, widespread, gas-saturated, fine-grained, organic rich units containing other types of organic matter, which were subjected to extensive biogenic degradation in the thermally immature stage or significant thermal decomposition in the thermally mature or over mature stages, can also serve as excellent exploration targets (Hamblin, 2006; Martini et al., 2003; Tan et al., 2015). The organic matter of the Carboniferous shales in South China have typically been regarded

as a type III kerogen (Luo, et al., 2012; Zhang et al. 2014) derived from terrestrial plants. In the Mississippian, organic material in paralic shale and coal seams were both derived from terrestrial plants, including Lycopsids and Equisetopsids (Gu et al., 2015; Zhang et al. 2014). However, the coal seams in the Longtan formation are locally distributed across central Hunan, and the shale with high TOC content does not tend to occur within coal seams (Ji et al., 2011). This might be the reason why the organic matter type of the Permian shale differs from that of the Carboniferous shale. Bao et al. (2016) reported that the kerogen $\delta^{13}C$ values in the Longtan and Dalong shales range from -23‰ to -27‰, further confirming that the organic matter is dominated by type II kerogen, with a minor component of type III kerogen.

Most shale gas that is currently produced is primarily a thermogenic gas that was formed by the thermal degradation of organic matter (Tan, et al., 2014c). For example, the highly productive Barnett shale gas play normally has a Ro >1%, while the Lower Silurian Longmaxi shale in South China has a Ro generally >2% (Chen et al., 2011; Tan, et al., 2015; Zhang et al., 2015). Although a minor fraction of shale gas might be of biogenic origin in the thermally immature stage (Martini et al., 2003; Martini et al., 2008), such quantities are significantly less than those of thermogenic shale gas (Tan, et al., 2014c). In addition to the current study, other studies have reported that Ro values of the Longtan and Dalong shales range from 1.1% to 2.4%, with a mean value of 1.6% (Bao et al., 2016; Gu et al., 2015). Zhang et al. (2014) have also documented that the Ro values of the Longtan shale range from 1.7% to 2.0%, with a mean value of 1.8%. Compared to the lower Cambrian and Lower Silurian marine shales in or adjacent to the Sichuan basin, which generally exhibit an equal Ro value >2.0%, the transitional shales studied here are less thermally mature. Interestingly, as shown in Tables 1 and 2, Ro values of the transitional shales increase gradually in strata that are stratigraphically older, indicating a burial depth control on thermal maturity.

#### 4.2.2 Mineralogical composition

To produce shale gas economically, horizontal drilling and hydraulic fracturing are the most popular choices for completing shale gas wells. The mineralogical composition of shale plays affects both the reservoir quality and well completion quality. Detailed characterization of the mineral constituents is thus critical to the identification of exploration targets, and essential for determining how the shale reservoir should be completed (Tan, et al., 2014b).

Mineral compositions are closely related to rock mechanics, and directly determine the brittleness of the rock. The brittleness of shale rocks reflects the capability to fail under pressure, and for cracks to remain open once the rock fractures (Rickman et al., 2008). Brittle shales thus generally respond well to well completion treatments. However, ductile shales, which might be fractured during hydraulic fracturing, can also be easily healed after stimulation. It has been recognized that quartz-rich and clay-low zones are commonly the most brittle intervals within a shale formation (Johnston, 2004). Hydraulic fracturing strategies used in the more brittle zones are reported to enhance the overall gas production of the well (Boyer et al., 2006). More specifically, Bowker (2002) has suggested that the brittle Barnett shale intervals are generally composed of 45% quartz, 27% illite, 8% carbonate, 7% feldspar, 5% pyrite, and 3% siderite.

One of the most common methods to determine the brittleness of a shale play is based on relative mineral compositions. Jarvie et al. (2007) and Rickman et al. (2008) documented the correlations between mineral composition and brittleness of the Barnett shales. They reported that the most brittle Barnett shales have high quartz contents, and low clay mineral contents. Conversely, the least brittle shales are rich in clay minerals, with relatively minor amounts of quartz. The shales with abundant carbonate are moderately brittle. However, from a stimulation perspective, not all quartz responses equally during well completion. The most effective quartz component for enhancing brittleness appears to be the recrystallized biogenic

opaline silica. Detrital quartz, on the contrary, appears to be less effective (Jarvie et al., 2007). The Brittleness Index was proposed based upon the relative proportions of quart group minerals (primarily quartz, feldspar, and pyrite), carbonates, and clay minerals, as: Brittleness Index=quartz/(quartz+carbonates+clays) (Jarvie et al., 2007). Selecting zones in a shale interval that are relatively more brittle is of importance for developing fractures that are large enough to connect the largest rock volume to the wellbore during the well completion process. The geometry of fractures created in brittle shales is different from that of ductile shales. The stimulation treatments carried out on brittle shales can create large, complex fracture networks that expose a large amount of shale surface area, and thus enable commercial gas production (Grieser and Bray, 2007).

Mineral compositions are also important for fluid selection during well completion. The determination of mineralogy and fluid sensitivity is essential for optimizing completion and stimulation strategies (Britt and Schoeffler, 2009). In most cases, acid is commonly used to dissolve soluble minerals, increase porosity, and improve the fracturing process. Because carbonate minerals can be easily dissolved even in weak acid solutions, the contents of carbonates evidently correlate with the acid solubility of shale samples (Rickman, et al., 2008). If samples have low carbonate concentrations, they generally show low to moderate acid solubility. In that scenario, mixed fluids of weak acids and surfactants are recommended to roughen the fracture surfaces, increase surface areas, and prevent significant generation of fines that could cause plugging of the fractures created, and damage to perforations (Rickman, et al., 2008). On the other hand, clay swelling is a significant problem for the stability of boreholes and created fractures, and finally on the gas recovery from shale reservoirs. If more smectite or illite/smectite mixed layers are present, the swelling potential of the shale might be substantial. In this case, development then requires more protective strategies, and more rigorous evaluation before the initiation of hydraulic fracturing.

The average quartz and clay mineral contents of Permian shales in South China are commonly >50%, and <25%, respectively (Zhang et al., 2016). Meanwhile, Carboniferous shales in the same region exhibit quartz and clay mineral contents of ~60.8% and ~23.3%, respectively (Miao et al. 2016). The highly productive lower Palaeozoic marine shales in South China and the transitional shales in Palaeozoic basins in North China generally contain highly brittle mineral contents (> 60% on average), and low clay mineral contents (< 40% on average) (Chen et al., 2011; Ding et al., 2013; Tan et al., 2014b; Tang et al., 2014; Zhang et al., 2015). Our study also indicates mineral compositions in transitional Carboniferous and Permian shales in South China that are dominated by brittle minerals. These findings could provide valuable insights for reservoir evaluation and stimulation treatments in the future.

4.2.3 Petrophysics

Intercrystallite pores in pyrite framboids commonly exist in shale samples, and contribute to gas storage (Loucks et al., 2009, 2012). For the analysed transitional shale intervals, pyrite was relatively abundant in shales from the Longtan formation, thus intraparticle pores occur more frequently (Fig. 5b). Intraparticle pores occur in shale samples with relatively high carbonate and/or feldspar contents (Figs. 5b–d). This can be ascribed to the partial dissolution of soluble carbonate and feldspar minerals (Heath, et al., 2011; Loucks et al., 2012). Microfractures (Figs. 5e), which can be formed during catagenesis, are well developed in shale samples with high clay mineral contents (i.e., illitisation could result in microfractures in shale with lengths up to tens of micrometres) (Liang et al., 2014).

Previous studies have shown that the average porosity and permeability of the Permian shales in the study area are <2% and ~0.007 mD, respectively (Gu et al., 2015; Bao et al., 2016), whereas the porosity of the Carboniferous Ceshui shale ranges from 1% to 6.2 %, with a mean value of 3.5% (Miao, et al., 2016). Compared with these results, porosity and permeability values obtained for the shale samples in our investigation are generally higher

(Table 3). One of the primary reasons might be that some of the shale samples in the current study have higher TOC contents, and well-developed micro-fractures. As our samples were freshly collected, weathering impact on petrophysical properties should be low. However, our findings suggest that these shale intervals are all characterized by low porosity and ultra-low permeability, which may result in an even tighter reservoir than the Barnett shale (Dong, et al., 2016).

To analyse the primary drivers of porosity formation, we examined the correlation between porosity and TOC content (Fig. 7a). There is a positive correlation between TOC content and porosity for most of the selected samples. This suggests that organic matter probably dominates the porosity of the shale. This might also be the reason why the porosity of the Longtan shale is comparatively higher than the less organic-rich shales from the Dalong and Ceshui formations (Table 3). Additionally, there is a negative relationship between the porosity and density (Fig. 7b). This phenomenon might be related to organic matter content because the density of shale tends to decrease as TOC contents increase (Fig. 7c). However, a few of the selected samples have higher porosity and permeability, even though they have relatively low TOC (e.g., sample LSJ05; Tables 2 and 3). Through SEM analysis, we found that these samples generally have well developed microfractures (e.g. LSJ05; see Fig. 5e). This could suggest that microfractures can be an important contributor to porosity. For the Barnett shale, microfractures provide migration pathways, and reservoir space for the accumulation of shale gas (Liang et al., 2014; Loucks et al., 2012). However, in this study, correlations between porosity and mineral constituents (e.g. quartz and clay minerals) of the shale remain unclear, and this is likely due to the heterogeneity of the shales.

In general, shales exhibit significant anisotropic properties from the nanometre scale to the reservoir scale (e.g., organic and inorganic constituents, mineral types, and structures). For low TOC samples, mineral-associated pores should be dominant. Nevertheless, the

contribution of organic matter host pores becomes significant if TOC content rises and thermal maturity increases to the gas window. According to research performed on the highly mature (dry gas window) Longmaxi shale in South China, most of the pores in that unit are mineral pores when TOC is less than 0.9%. The contribution of mineral pores is similar to that of organic pores when TOC is in the range of 0.9-1.7%, and organic pores are more significant than mineral pores when TOC is higher than 1.7% (Tang et al., 2016). However, the Barnett shale samples that span a maturity range from a later wet gas window to a dry gas window indicate a positive correlation between TOC and porosity for samples with TOC <5.5%, and little or no correlations for samples with TOC >5.5% (Milliken, et al., 2013). Since quartz, carbonates, and clay minerals are the principal mineral constituents of shales, their relative concentrations can significantly influence porosity because clay minerals are porous, while carbonates can be easily dissolved by geofluids (Ross and Bustin, 2009). In some shales, the pyrite content can be greater than 10%, and pyrite framboids are commonly present. In that context, pyrite-associated pores may also be important.

Shales are slowly deposited through suspension in calm waters, and this long deposition period can result in strong vertical heterogeneity in both composition and structure. Lamina, thin sand layers, and bioclasts all vary over time in the investigated shale intervals. As revealed by Pan et al. (2015b), in addition to organic and inorganic constituents, the heterogeneous layering structures in different directions in shales strongly impact porosity and permeability, resulting in anisotropic petrophysical properties. However, porosity and permeability measurements are generally performed on small sample pieces or plugs, and the obtained results are very sensitive to experimental conditions. Therefore, accounting for the petrophysical properties of shales at a large scale requires a very large sample size from across the vertical and spatial extents of the unit. Additional studies with larger sample sizes are needed in the future.

4.2.4 Methane adsorption capacity

Research by Bao et al. (2016) has previously shown that the average methane adsorption capacity of the Permian Longtan and Dalong shales are 2.7 and 3.5 $cm^3/g$, respectively, exhibiting a relatively strong gas adsorptive potential. Nevertheless, the Carboniferous-Permian shale intervals have lower methane adsorption capacity compared to the lower Cambrian and lower Silurian marine shales in or adjacent to the Sichuan basin, South China (Tan et al., 2014a; Zhang et al., 2015). The gas adsorption capacity of over mature marine shales is positively correlated with TOC content (Chalmers et al., 2008; Gasparik et al., 2014; Han et al., 2013; Tan et al., 2014a; Wu et al., 2014). However, as shown in Fig. 7, the methane adsorption capacity of TOC-rich samples (i.e. DLS02 and DBQ09) is not always significantly higher than that of TOC-poor samples (i.e. NT02) for the high maturity shales of this study. This suggests that other factors may play more important roles in influencing methane adsorption.

Shale samples with Ro values less than 1.5% (i.e., samples DLS02 and DBQ09; Fig. 6) have low gas adsorption capacity irrespective of their TOC values. However, when Ro values of the shale samples are greater than 1.5% (i.e., samples NT02 and JZS09; Fig. 6), their gas adsorption capacity is much higher than that of the shale samples with Ro values <1.5%. This suggests that the gas adsorption capacity might be closely associated with thermal maturity for the high maturity shales. Compared with the two samples with Ro values above 1.5% (i.e., samples DLS02 and DBQ09; Fig. 6), even when there is little difference in thermal maturity, the gas adsorption capacity of the shale increases greatly with higher TOC content. This implies that the organic matter content might be largely responsible for adsorbing gas in the high maturity range.

Micropores hosted in organic matter are the primary factor that influences the adsorption capacity of organic-rich rocks (Loucks, et al., 2012; Tan, et al., 2014a; Tan, et al.,

2014b; Zhang et al., 2015; Zhong et al., 2016). However, micropores are poorly developed during the low maturity to oil window range (Ro=0.5-1.0%) but increase dramatically as thermal maturity enters the gas window stage (Ro ≥1.5%) (Xiong et al., 2015). Additionally, organic matter type possibly influences the adsorption capacity of shale and coal samples (Gasparik et al., 2014; Tan et al., 2014a;). The transitional shales in the current study contain moderate amounts of type III organic matter, while the lower Cambrian and lower Silurian marine shales in South China lack type III kerogen. The relatively lower adsorption capacity of the analysed transitional shales can be partially ascribed to the different types of organic matter.

The Xiangye-1 well in the study area is the first and, presently, the only natural gas exploration well targeted toward the studied transitional shales (Bao et al., 2016; Gu et al., 2015). During drilling, the Dalong formation shale exhibited very low desorption gas content that was attributed to poor preservation conditions, long periods of tectonic alteration, and extensive thermal evolution (Bao et al., 2016; Gu et al., 2015). Based on the above discussion, the low gas content might also result from the low thermal maturity given that shales with Ro <1.5% generally have less gas adsorption capacity. As shown in Tables 1 and 2, the Ro values for most of the Dalong formation shale samples are <1.5%. The intrinsic reason is that micropores might be relatively less developed in a low thermal maturity range. It should be noted that extrapolations from adsorption data obtained in the lab to *in situ* subsurface geological conditions requires a more comprehensive, multi-factor analysis.

In addition to the inherent properties of shales (e.g., organic matter content, mineral constituents, thermal maturity, and pore structure), *in situ* geological conditions of shale reservoirs are fraught with uncertainties. For example, gas adsorption measurements are generally performed in isothermal conditions, whereas the geological temperature varies in reservoirs at different depths. The simulated applied pressure is likely much lower than actual

reservoir pressures, given that the burial depth of some of the shale gas reservoirs in South China exceeds 5 km. The moisture content also varies markedly with diagenesis and thermal maturation of organic matter. Moreover, gas adsorption measurements are commonly performed on cuttings or powders that show higher pore surface accessibility than the intact shales underground.

Nevertheless, experimental adsorption data provide the basis for GIP estimation, particularly for regions where natural gas production has not yet been achieved, and desorption data are very rare (Gasparik, et al., 2014). The uncertainty of GIP estimation resulting from both inherent and exogenic factors can be controlled through adsorption experiments performed on a number of representative samples, and under a variety of lab conditions, and with enhanced knowledge of the *in situ*, underground geological conditions of shale reservoirs (Gasparik, et al., 2014).

## 5. Conclusions

We conducted a variety of analyses on Carboniferous and Permian transitional shale samples from central Hunan to investigate their natural gas potential. Our primary findings are:

1. These shale intervals are abundant in organic matter and were deposited in reducing sedimentary environments. The organic matter type of the Ceshui shale is dominated by type III kerogen, while that of the Permian shale is principally type II. The thermal maturities of the shales have entered into the late wet gas and dry gas window stages, respectively.
2. Non-laminated and carbonaceous shale are the dominant lithological types, followed then by calcareous shale, silty shale, and siliceous shale. Quartz and clay minerals are

the principal constituents. Pyrite is highly concentrated in certain Permian shale samples, and generally coincides with higher TOC contents.

3. Four types of pore structures were identified through SEM analysis (i.e., organic matter pores, interparticle pores, intraparticle pores, and microfractures). The mean porosity for all sample is 6.4%, and the mean permeability is 0.013 mD. TOC and well-developed microfractures can greatly affect the porosity and permeability of the shale.
4. The gas adsorption capacity of the transitional shales was found to vary from 1.24 $cm^3/g$ to 4.53 $cm^3/g$, with a mean value of 2.40 $cm^3/g$ under the experimental conditions. Meanwhile, shales with high TOC content and Ro >1.5% exhibit high gas adsorption capacity.

**Acknowledgements**

This work is supported by the Open Fund (PLC201302) of the State Key Laboratory of Oil and Gas Reservoir Geology and Exploitation (Chengdu University of Technology), Major Project of Hunan Provincial Science and Technology Bureau (2012FJ1006), the Open Fund (E21645) of the Hunan Key Laboratory of Shale Gas Resource Utilization (Hunan University of Science and Technology), and the Innovation Program of Central South University (502501005). We thank Jeffrey Dick for editing the language. Zhenghui Xiao also acknowledges support from the China Scholarship Council (CSC).

**Appendix**

1. Type III kerogen is derived from terrestrial plant debris, much of which remains taxonomically identifiable. Additionally, type III kerogens mostly contain condensed

polyaromatics and oxygenated functional groups, with minor aliphatic chains (Tissot and Welte, 1984).

2. Type II kerogen is typically derived from a mixture of phytoplankton, zooplankton, and microorganisms (bacteria) that have been deposited in a reducing environment. Though type II kerogens may also include terrestrial debris (pollen spores, plant cuticle, etc.), they are most often found in marine sediments characterized by autochthonous organic matter (Tissot and Welte, 1984).

**References**

Bao, S.J., Lin, T., Nie, H.K., Ren, S.M., 2016. Preliminary study of the transitional facies shale gas reservoir characteristics: Taking Permian in the Xiangzhong Depression as an example. *Earth Science Frontiers* 23, 44–53.

Bowker, K.A., 2007. Barnett Shale gas production, Fort Worth Basin: issues and discussion. *AAPG Bulletin* 91, 523–533.

Boyer C, Kieschnick J, Lewis R., 2006. Producing gas from its source. *Oilfield Review*, 18, 36-49.

Britt, L., Schoeffler, J., 2009. The geomechanics of a shale play: What makes a shale prospective. In SPE Eastern Regional Meeting. *Society of Petroleum Engineers* 125525, 1-9.

Bu, H., Ju, Y., Tan, J., Wang, G., & Li, X., 2015. Fractal characteristics of pores in non-marine shales from the Huainan coalfield, eastern China. *Journal of Natural Gas Science and Engineering* 241, 66-177.

Chalmers, G.R.L., Bustin, R. M., 2008. Lower Cretaceous gas shales in northeastern British Columbia. Part I: Geological controls on methane sorption capacity. *Bulletin of Canadian petroleum geology* 56, 1–21.

568 Chen, S.B., Zhu, Y.M., Wang, H.Y., Liu, H.L., Wei, W., Fang, J.H., 2011. Shale gas
569 reservoir characterization: a typical case in the southern Sichuan Basin of China. *Energy*
570 36, 6609–6616.
571 Dang, W., Zhang, J.C., Tang, X., Chen, Q., Han, S.B., Li, Z.M., Du, X.R., Wei, X.L., Zhang,
572 M.Q., Liu, J., Peng, J.L., Huang, Z.L., 2016. Shale gas potential of Lower Permian
573 marine–continental transitional black shales in the Southern North China Basin, central
574 China: Characterization of organic geochemistry. *Journal of Natural Gas Science and*
575 *Engineering* 28, 639–650.
576 Ding, W.L., Zhu, D.W., Cai, J.J., Gong, M.L., Chen, F. Y., 2013. Analysis of the
577 developmental characteristics and major regulating factors of fractures in marine–
578 continental transitional shale–gas reservoirs: A case study of the Carboniferous–Permian
579 strata in the southeastern Ordos Basin, central China. *Marine and Petroleum Geology* 45,
580 121–133.
581 Dong, D.Z., Wang, Y.M., Huang, X.N., Zhang, C.C., Guan, Q.Z., Huang, J.L., Wang, S.F., Li,
582 X.J., 2016. Discussion about geological characteristics, resource evaluation methods and
583 its key parameters of shale gas in China. *Natural Gas Geoscience* 27, 1583–1601.
584 Feng, Z.Z., He, Y.B., Wu, S.H., 1993. Lithofacies paleogeography of Permian Middle and
585 Lower Yangtze region. *Acta Sedimentologica Sinica* 11, 13–24.
586 Gasparik, M., Bertier, P., Gensterblum, Y., Ghanizadeh, A., Krooss, B. M., Littke, R., 2014.
587 Geological controls on the methane storage capacity in organic–rich shales. *International*
588 *Journal of Coal Geology* 123, 34–51.
589 Grieser, W., Bray, J. 2007. Identification of Production Potential in Unconventional
590 Reservoirs. Society of Petroleum Engineers. doi:10.2118/106623-MS

591 Gu, Z.X., Peng, Y.M., He, Y.B., Hu, Z.Q.; Zhai, Y.J., 2015. Geological conditions of
592 Permian sea–land transitional facies shale gas in the Xiangzhong depression. *Geology in*
593 *China* 42, 288–299.
594 Hamblin, A.P., 2006. The "Shale Gas" concept in Canada: A preliminary inventory of
595 possibilities. *Geological Survey of Canada* 5384:108.
596 Han, S.B., Zhang, J.C., Li, Y.X., Horsfield, B., Tang, X., Jiang, W.L., Chen, Q., 2013.
597 Evaluation of lower Cambrian shale in Northern Guizhou Province, South China:
598 implications for shale gas potential. *Energy & Fuels* 27, 2933–2941.
599 He, J.H., Ding, W.L., Zhang, J.C., Li, A., Zhao, W., Dai, P., 2016. Logging identification and
600 characteristic analysis of marine–continental transitional organic–rich shale in the
601 Carboniferous–Permian strata, Bohai Bay Basin. *Marine and Petroleum Geology* 70, 273–
602 293.
603 Heath J.E., Dewers T.A., McPherson B.J., Petrusak R., Chidsey, Jr. T.C., Rinehart A.J.,
604 Mozley, P.S., 2011. Pore networks in continental and marine mudstones: Characteristics
605 and controls on sealing behavior. *Geosphere* 7, 429–454.
606 Jarvie, D.M., Hill, R.J., Ruble, T.E., Pollastro, R.M., 2007. Unconventional shale–gas
607 systems: the Mississippian Barnett Shale of north–central Texas as one model for
608 thermogenic shale–gas assessment. *AAPG Bulletin* 91, 475–499.
609 Ji, C.W., Shao, L.Y., Peng, Z.Q., 2011. Late permian sequence–paleogeography and coal
610 accumulation in Hunan province. *Journal of China University of Mining & Technology* 40,
611 103–110.
612 Ji, W. M., Song, Y., Jiang, Z. X., Wang, X.Z., Bai, Y.Q., Xing, J. Y., 2014. Geological
613 controls and estimation algorithms of lacustrine shale gas adsorption capacity: a case study
614 of the Triassic strata in the southeastern Ordos Basin, China. *International Journal of Coal*
615 *Geology* 134, 61-73.

Jing, L., Pan, J.P., Xu, G.S., Ma, R.L., Yuan, H.F., Luo, X.P., Wu, C.R., 2013. Lithofacies paleogeography characteristics of the marine shale series of strata in the Xiangzhong–Xiangdongnan depression, Hunan, China. *Journal of Chengdu University of Technology* 39, 215–222.

Johnston, D., 2004. Technological advances expand potential pay. *Oil and Gas Journal*, 102, 51-59.

Li, G.L., Wang, X.H., Bo, D.Y., Luo, P., Jiang, W., 2015. Potentiality exploration of the Upper Permian Longtan formation shale gas in central and southeastern Hunan Province. *Geological Science and Technology Information* 34, 133–138.

Li, H.T., Cao, D.Y., Wang, L.J., Guo, A.J., Li, Y.F., Xu, Hao. 2013. Characteristics and evolution of coal-controlled structures on the east slope of the Xuefengshan Domain in central Hunan province. *Geotectonica et Metallogenia* 37,611-621.

Liang, C., Jiang, Z.X., Zhang, C.M., Guo, L., Yang, Y.T., Li, J., 2014. The shale characteristics and shale gas exploration prospects of the Lower Silurian Longmaxi shale, Sichuan Basin, South China. *Journal of Natural Gas Science & Engineering* 21, 636–648.

Liang, J.J., Ma, R.L., Bu, S.F., Liu, W.J., Yang, C., 2014. Reservoir characteristics of shale in Xiangzhong depression and Xiangdongnan depression of Hunan, China. *Journal of Chengdu University of Technology* 41, 45–54.

Loucks, R. G., Reed, R. M., Ruppel, S. C., Jarvie, D. M., 2009. Morphology, genesis, and distribution of nanometer-scale pores in siliceous mudstones of the Mississippian Barnett Shale. *Journal of Sedimentary Research* 79, 848−861.

Loucks, R.G., Reed, R.M., Ruppel, S.C., Hammes, U., 2012. Spectrum of pore types and networks in mudrocks and a descriptive classification for matrix–related mudrock pores. *AAPG Bulletin* 96, 1071–1098.

641 Luo, X.P., Liu, J., Xu, G.S., Ma, R.L., Xian, Z.Y., Xu, M., 2012. Geochemical characteristics
642 and isothermal adsorption properties of the Devonian–Carboniferous marine mud shale in
643 the Xiangzhong depression, Hunan, China. *Journal of Chengdu University of*
644 *Technology* 39, 206–214.
645 Martini, A. M., Walter, L. M., McIntosh, J. C., 2008. Identification of microbial and
646 thermogenic gas components from Upper Devonian black shale cores, Illinois and
647 Michigan basins. *AAPG Bulletin* 92, 327-339.
648 Martini, A.M., Walter, L.M., Ku, T.C.W., Budai, J.M., McIntosh, J.C., Schoell, M., 2003.
649 Microbial production and modification of gases in sedimentary basins: A geochemical
650 case study from a Devonian shale gas play, Michigan basin. *AAPG Bulletin* 87, 1355–
651 1375.
652 Pan, Z. and Connell, L.D. 2015. Reservoir simulation of free and adsorbed gas production
653 from shale. *Journal of Natural Gas Science and Engineering* 22, 359-370.
654 Pan, Z., Ma, Y., Connell, L. D., Down, D. I., and Camilleri, M. 2015. Measuring anisotropic
655 permeability using a cubic shale sample in a triaxial cell. *Journal of Natural Gas Science*
656 *and Engineering*, 26, 336-344.
657 Rickman, R., Mullen, M. J., Petre, J. E., Grieser, W. V., & Kundert, D. 2008. A practical use
658 of shale petrophysics for stimulation design optimization: All shale plays are not clones of
659 the Barnett Shale. Society of Petroleum Engineers. doi:10.2118/115258-MS
660 Shao, L.Y., Zhang, P.F., Liu, Q.F., Zheng, M.J., 1992. The Lower Carboniferous Ceshui
661 Formation in central Hunan, South China: depositional sequences and episodic coal
662 accumulation. *Geological Review* 38, 52–58.
663 Slatt, R.M., O'Brien, N.R. 2011. Pore types in the Barnett and Woodford gas. *AAPG Bulletin*
664 95, 2017–2030.

665 Tan, J. Q., Weniger, P., Krooss, B., Merkel, A., Horsfield, B., Zhang, J. C., Boreham, C. J.,
666 Graas, G. V., Tocher, B. A., 2014a. Shale gas potential of the major marine shale
667 formations in the Upper Yangtze Platform, South China, Part II: Methane sorption
668 capacity, *Fuel* 129, 204−218.
669 Tan, J.Q., Horsfield, B., Fink, R., Krooss, B., Schulz, H. M., Rybacki, E., Zhang, J.C.,
670 Boreham, C. J., Graas, G.V., Tocher, B.A., 2014b. Shale gas potential of the major marine
671 shale formations in the Upper Yangtze platform, South China, Part III: mineralogical,
672 lithofacial, petrophysical, and rock mechanical properties. *Energy Fuels* 28, 2322–2342.
673 Tan, J.Q., Horsfield, B., Mahlstedt, N., Zhang, J.C., diPrimio, R., Vu, T. A. T., Boreham,
674 C. J., Graas, G. V., Tocher, B. A., 2013. Physical properties of petroleum formed during
675 maturation of Lower Cambrian shale in the upper Yangtze Platform, South China, as
676 inferred from PhaseKinetics modelling. *Marine & Petroleum Geology* 48, 47–56.
677 Tan, J.Q., Horsfield, B., Mahlstedt, N., Zhang, J.C., Boreham, C. J., Hippler, D., Graas, G. V.,
678 Tocher, B. A., 2015. Natural gas potential of Neoproterozoic and lower Palaeozoic marine
679 shales in the Upper Yangtze Platform, South China: geological and organic geochemical
680 characterization. *International Geology Review* 57, 305-326.
681 Tang, S., Zhang, J.C., Elsworth, D., Tang, X., Li, Z. M., Du, X. R., Yang, X.Q., 2016.
682 Lithofacies and pore characterization of the Lower Permian Shanxi and Taiyuan shales in
683 the southern North China Basin. *Journal of Natural Gas Science & Engineering* 36, 644–
684 661.
685 Tang, X., Zhang, J.C., Wang, X.Z., Yu, B.S., Ding, W.L., Xiong, J.Y., Yang, Y.T., Wang,
686 L.,Yang, C., 2014. Shale characteristics in the southeastern Ordos Basin, China:
687 implications for hydrocarbon accumulation conditions and the potential of continental
688 shales. *International Journal of Coal Geology* 128, 32–46.
689 Tissot B P, Welte D H. 1984. Petroleum Formation and Occurrence. Springer-Verlag, 1984.

690 Wang, J., Li, S.Z., Jin, C., Wang, Y.J., Zhang, G.W., Liu, L.P., Liu, X. 2010. Dome-and-
691 basin pattern in central Hunan province: stages and genesis of fold superposition.
692 *Geotectonica et Metallogenia* 34, 159-165.
693 Wang, M.Y., Guo, J.L., Kuang, L.X., Zhu,T., 2010. Geochemical characteristics and
694 evolution of the hydrocarbon source rocks from Lianyuan Depression in the middle of
695 Hunan province. *Natural Gas Geoscience* 21, 721–726.
696 Wu, Y., Fan, T.L., Zhang, J.C., Jiang, S., Li, Y.F., Zhang, J.P., Xie, C., 2014.
697 Characterization of the upper Ordovician and lower Silurian marine shale in northwestern
698 Guizhou province of the upper Yangtze block, South China: Implication for shale gas
699 potential. *Energy Fuels* 28, 3679–3687.
700 Xiong, J.Y., Li, S.T., Tang, X., Chen, R.Y., Wang, M., Huang, Z.L., Sun, X.N., Du, K.F,
701 2015. Organic matter occurrence and microscopic mechanism of pore formation in the
702 lacustrine tight carbonate reservoirs. *Oil & Gas Geology* 36, 756–765.
703 Xu, F.H., Qian, J., Yuan, H.F., Xu, G.S., Liang, J.J., 2015. Sedimentary mode and reservoir
704 properties of mud shale series of strata in Xiangzhong–Xiangdongnan depression, Hunan,
705 China. *Journal of Chengdu University of Technology* 42, 80–89.
706 Xu, Y.G., Qi, K.L., 2005. Reconsideration on marine petroleum exploration prospects in the
707 middle Hunan depression. *Petroleum Geology & Expeximent* 27, 594–596.
708 Zhan, G.J., Liu, G.X., Guan, H.L., Fang, C.M, Deng, M., 2006. Genetic types of natural gas
709 of Xiangzhong depression. *Natural Gas Geoscience* 21, 721–726.
710 Zhang, C.L., Tang, S.H., Fan, E.P., Wang, S.B., Sun, C.H., Sun, J.J., 2014. Shale gas
711 reservoir characteristics of Longtan Formation in Lianyuan Depression. *Journal of Oil &*
712 *Gas Technology* 36, 32–36.

713 Zhang, G, T, Chen, X, H,, Zhang, B. M., Li, H., 2016. Physical property characteristics of
714 Permian shale reservior in the Shaoyang Depression, central Hunan province.
715 *Geology and Mineral Resources of South China* 32, 149–158.
716 Zhang, J.P., Fan, T.L., Li, J., Zhang, J.C., Li, Y.F, Wu, Y., Xiong, W.W., 2015.
717 Characterization of the Lower Cambrian Shale in the Northwestern Guizhou Province,
718 South China: Implications for Shale–Gas Potential. *Energy Fuel* 29, 6383–6393.
719 Zhang, L.T., Guo, J.H., Jiao, P., Zhang, Z., 2014. Accumulation conditions and exploration
720 potential of shale gas of Lower Carboniferous in Lianyuan Depression in the middle of
721 Hunan Province. *Journal of Central South University* 45, 2268–2277.
722 Zhong, J.A., Chen, G.J., Lv, C.F., Yang, W., Xu, Y., Yang, S., Xue, L.H., 2016.
723 Experimental study of the impact on methane adsorption capacity of continental shales
724 with thermal evolution. *Journal of Natural Gas Geoscience* 1, 165–172.
725 Zhou, X.K., Guo, J.H., 2014. Petroleum accumulation characteristics and preservation
726 conditions of Lianyuan sag in the central Hunan. *Journal of Geomechanics* 20, 222–229.
727 Zhu, W., Yi, J.Z., 2012. Analyses on the complex geologic structure and its gas exploration
728 potential in Lianyuan region of middle Hunan province. *Special Oil & Gas Reservoirs* 19,
729 35–38.
730 Zou, C.N., Dong, D.Z., Wang, S.J., Li, J.Z., Li, X.J., Wang, Y.M., Li, D.H., Chen, K.M.,
731 2010. Geological characteristics, formation mechanism and resource potential of shale gas
732 in China. *Petroleum Exploration and Development* 6, 641–653.
733

734 **Fig. 1.** (a) Outline map of China showing position of Hunan Province and study area. (b)
735 Regional geological map of the study area and sampling locations. (c) Generalized
736 stratigraphic column of Carboniferous-Permian strata of the study area with stars marking
737 position of target shales (modified from Jing et al., 2013).

738

739 **Fig**. 2. Structural geology map of central Hunan (Modified from Li et al. 2013)

740

741 **Fig. 3.** Ternary diagram of mineralogical constituents.

742

743 **Fig. 4.** Petrological images of Carboniferous-Permian transitional shale samples from the
744 study area. (a) Calcareous shale (QXJ05) from the Lopingian aged Dalong formation at the
745 Qixingjie section. Quartz and carbonate concentrate in white laminae, while clay and organic
746 matter concentrate in black laminae. (b) Non-laminated shale (DPQ06) from the Lopingian
747 aged Dalong formation at the Duanpoqiao section; dark area is mainly composed of organic
748 matter and clay, while the light area primarily comprises quartz and feldspar. (c) Non-
749 laminated shale (NT02) from the Lopingian aged Longtan at the Nantang section; dark area
750 consists of organic matter and clay, and the light is mainly quartz. (d) Carbonaceous shale
751 (DLS05) from the Lopingian aged Longtan formation at the Doulishan section; dark area is
752 mainly organic matter and clay, and the light is mainly quartz and feldspar. (e) Silty shale
753 (LMJ06) from the Mississippian aged Ceshui formation at the Lumaojiang section; clay
754 minerals occupy a large area in the texture, while organic matter and quartz are scattered
755 amongst the matrix. (f) Carbonaceous shale (LSJ04) from the Mississippian aged Ceshui
756 formation at the Liangshuijing section; dark area is mainly organic matter and light area is
757 mainly quartz. Organic matter aggregates or particles are randomly distributed in the matrix.

758

759 **Fig. 5.** SEM images of Carboniferous–Permian transitional shale samples from the study
760 area. (a) Carbonaceous shale (LSJ04) from the Mississippian aged Ceshui formation at the
761 Liangshuijing section; “honeycomb” organic pores and micro-fractures are well developed.
762 (b) Carbonaceous shale (DLS05) from the Lopingian aged Longtan formation at the

Doulishan section; interparticle pores exist between pyrite framboids or between pyrite crystals and clay flakes. Intra–particle pores in the feldspar minerals and "honeycomb" organic–matter pores generated by hydrocarbon expulsion are well developed. (c) Calcareous shale (QXJ02) from the Lopingian aged Dalong formation at the Qixingjie section; intraparticle pores in the carbonate minerals are well developed. (d) Transitional shale (DPQ03) from the Lopingian aged Dalong formation at the Duanpoqiao section; inter–particle pores occur between quartz minerals, intra–particle pores exist in the feldspar minerals and micro-fractures in clay minerals and at weak interfaces are well developed. (e) Carbonaceous shale (LSJ05) from the Mississippian aged Ceshui formation at the Liangshuijing section; micro-fractures between clay flakes or between clay laminae and silty laminae are well developed. (f) Silty shale (LMJ06) from the Mississippian aged Ceshui formation at the Lumaojiang section; micro-fractures between clay flakes are well developed.

**Fig. 6.** Methane adsorption isotherms at 40 °C

**Fig. 7.** Correlation plots for Carboniferous-Permian shale samples in Central Hunan Province plotting (a) porosity with TOC content, (b) porosity with density, and (c) TOC content with density.

**Table 1.** TOC and Ro values from the Carboniferous–Permian transitional shale in central Hunan.

**Table 2.** Results of TOC, Ro and XRD mineralogy for some representative transitional shale samples from central Hunan.

788 **Table 3.** Rock density, porosity, and permeability for Carboniferous–Permian transitional
789 shale in central Hunan.

790

791 **Table 4.** Comparison of the shale gas reservoir rocks in central Hunan with other worldwide
792 shale gas source rocks. Setting = depositional environment of source rocks; TOC – Total
793 Organic Carbon; Kerogen = Kerogen Type; Ro = Vitrinite reflectance values; GAC = Gas
794 adsorbtion capacity. Data for Ceshui, Dalong and Longtan shales from this paper; sources for
795 other data from the study by Dong et al. (2016).

# Tables

Table 1. TOC and Ro of Carboniferous–Permian shale in central Hunan

| Formation | Sections(code) | TOC (%) | | | Ro (%) | | |
|---|---|---|---|---|---|---|---|
| | | Min value | Max value | Mean value | Min value | Max value | Mean value |
| Dalong | Shimingqiao(SMQ) | 0.4 | 5.0 | 3.3 | 1.1 | 1.4 | 1.3 |
| Dalong | Qixingjie(QXJ) | 0.6 | 4.6 | 2.3 | 1.2 | 1.7 | 1.4 |
| Dalong | Duanpoqiao(DPQ) | 0.9 | 6.6 | 4.8 | 1.2 | 1.8 | 1.5 |
| Dalong | Tantou(TT) | 0.5 | 4.8 | 2.2 | 1.2 | 1.7 | 1.5 |
| avg. | | 0.6 | 5.3 | 3.2 | 1.2 | 1.7 | 1.4 |
| Longtan | Qixingjie(QXJ) | 0.8 | 8.8 | 4.4 | 1.2 | 1.9 | 1.5 |
| Longtan | Doulishan(DLS) | 6.9 | 8.8 | 7.8 | 1.4 | 1.5 | 1.4 |
| Longtan | Nantang(NT) | 2.4 | 5.3 | 4.0 | 1.1 | 1.6 | 1.4 |
| Longtan | Jilong(JL) | 2.6 | 9.2 | 6.0 | 1.6 | 1.9 | 1.7 |
| Longtan | Tantou(TT) | 1.8 | 6.2 | 3.6 | 1.1 | 1.9 | 1.6 |
| avg. | | 2.9 | 7.7 | 5.2 | 1.3 | 1.8 | 1.5 |
| Ceshui | Jingzhushan(JZS) | 0.8 | 6.1 | 2.4 | 1.3 | 2.8 | 1.8 |
| Ceshui | Zhaoyang(ZY) | 2.2 | 9.0 | 4.5 | 1.6 | 2.2 | 1.9 |
| Ceshui | Liangshuijing(LSJ) | 0.4 | 7.4 | 1.8 | 1.5 | 2.4 | 2.1 |
| Ceshui | Xiandong(XD) | 0.4 | 1.6 | 1.2 | 1.4 | 1.8 | 1.7 |
| Ceshui | Lumaojiang(LMJ) | 0.7 | 2.0 | 1.3 | 1.2 | 1.9 | 1.5 |
| Ceshui | Douling(DL) | 0.8 | 3.6 | 2.4 | 1.4 | 2.0 | 1.8 |
| avg. | | 0.9 | 5.0 | 2.3 | 1.4 | 2.2 | 1.8 |

Table 2. Results of TOC, Ro and XRD mineralogy for some representative shale samples

| ID | Formation | samples | Lithofacies | TOC (%) | Ro (%) | quartz (%) | feldspar (%) | carbonate (%) | pyrite (%) | clay (%) |
|---|---|---|---|---|---|---|---|---|---|---|
| 1 | Dalong | QXJ02 | Calcareous shale | 0.6 | 1.7 | 39.1 | 0.0 | 35.2 | 0.0 | 25.7 |
| 2 | Dalong | QXJ05 | Calcareous shale | 4.6 | 1.2 | 50.6 | 0.0 | 30.0 | 1.3 | 18.1 |
| 3 | Dalong | QXJ08 | black siliceous shale | 3.2 | 1.2 | 86.2 | 2.8 | 0.0 | 0.0 | 11.0 |
| 4 | Dalong | DPQ02 | Calcareous shale | 0.9 | 2.0 | 52.6 | 4.6 | 32.7 | 0.0 | 10.1 |
| 5 | Dalong | DPQ03 | black shale | 5.9 | 1.8 | 43.8 | 12.5 | 1.6 | 0.0 | 42.1 |
| 6 | Dalong | DPQ06 | black shale | 6.1 | 1.5 | 79.3 | 4.4 | 0.0 | 4.3 | 12 |
| 7 | Dalong | DQ09 | black shale | 6.3 | 1.3 | 53.8 | 1.4 | 0.0 | 13.1 | 31.7 |
| 8 | Longtan | DLS02 | black carbonaceous shale | 8.8 | 1.4 | 47.6 | 14.2 | 0.0 | 13.1 | 25.1 |
| 9 | Longtan | DLS05 | black carbonaceous shale | 6.9 | 1.5 | 48.9 | 4.3 | 0.0 | 8.9 | 37.9 |
| 10 | Longtan | NT02 | black shale | 3.2 | 1.6 | 64.6 | 0.0 | 0.0 | 0.0 | 35.4 |
| 11 | Longtan | NT03 | black shale | 3.1 | 1.5 | 70.3 | 0.0 | 0.0 | 0.0 | 29.7 |
| 12 | Longtan | QXJ10 | black carbonaceous shale | 8.2 | 1.8 | 50.8 | 0.0 | 0.0 | 9.2 | 40.0 |
| 13 | Longtan | QXJ14 | black shale | 3.5 | 1.4 | 50.0 | 2.4 | 0.0 | 1.0 | 46.6 |
| 14 | Ceshui | XD01 | dark–grey shale | 1.5 | 1.8 | 53.7 | 0.0 | 0.0 | 0.0 | 46.3 |
| 15 | Ceshui | XD06 | dark–grey shale | 0.4 | 1.7 | 62.9 | 0.5 | 1.1 | 0.0 | 35.5 |
| 16 | Ceshui | JZS05 | dark–grey shale | 1.4 | 2.4 | 60.4 | 0.0 | 0.0 | 0.0 | 39.6 |
| 17 | Ceshui | JZS07 | dark–grey shale | 1.3 | 1.6 | 54.4 | 0.0 | 0.0 | 0.0 | 45.6 |
| 18 | Ceshui | JZS09 | black carbonaceous shale | 6.1 | 1.7 | 29.2 | 0.0 | 1.7 | 0.0 | 69.1 |
| 19 | Ceshui | LMJ02 | dark–grey shale | 1.2 | 1.6 | 52.2 | 0.0 | 0.0 | 0.0 | 47.8 |
| 20 | Ceshui | LMJ06 | silty shale | 0.7 | 1.7 | 39.0 | 0.0 | 0.0 | 3.7 | 57.3 |
| 21 | Ceshui | ZY04 | black shale | 2.3 | 2.0 | 50.9 | 0.0 | 0.7 | 8.6 | 39.8 |
| 22 | Ceshui | ZY08 | Calcareous shale | 2.2 | 2.1 | 19.3 | 0.0 | 48.2 | 4.8 | 27.7 |
| 23 | Ceshui | LSJ01 | black carbonaceous shale | 10.7 | 2.0 | 63.7 | 0.0 | 0.0 | 0.0 | 36.3 |
| 24 | Ceshui | LSJ04 | black carbonaceous shale | 7.4 | 2.1 | 60.0 | 0.0 | 0.0 | 0.0 | 40.0 |
| 25 | Ceshui | LSJ05 | dark–grey shale | 0.4 | 2.4 | 61.5 | 0.0 | 0.0 | 0.0 | 38.5 |

Table 3. Rock Density, Porosity, and Permeability for Carboniferous–Permian shale in central Hunan

| ID | Formation | samples | TOC (%) | Rock density (g/cm$^3$) | Porosity (%) | Permeability (mD) |
|---|---|---|---|---|---|---|
| 1 | Dalong | QXJ02 | 0.6 | 2.60 | 0.5 | 0.0032 |
| 2 | Dalong | QXJ05 | 4.6 | 2.53 | 5.2 | 0.0040 |
| 4 | Dalong | DPQ02 | 0.9 | 2.51 | 4.2 | 0.0031 |
| 5 | Dalong | DPQ03 | 5.9 | 2.62 | 5.1 | 0.0072 |
| 6 | Dalong | DPQ06 | 6.1 | 1.49 | 12.0 | 0.0470 |
| 7 | Dalong | DPQ09 | 6.3 | 2.40 | 6.9 | 0.0026 |
| 8 | Longtan | DLS02 | 8.8 | 1.66 | 14.0 | 0.0067 |
| 9 | Longtan | DLS05 | 6.9 | 1.78 | 8.2 | 0.0089 |
| 10 | Longtan | NT02 | 3.2 | 1.45 | 5.6 | 0.0034 |
| 11 | Longtan | NT03 | 3.1 | 1.46 | 9.2 | 0.0250 |
| 15 | Ceshui | XD06 | 0.4 | 2.60 | 1.4 | 0.0045 |
| 16 | Ceshui | JZS05 | 1.4 | 2.57 | 2.3 | 0.0034 |
| 22 | Ceshui | ZY08 | 2.2 | 2.53 | 4.7 | 0.0046 |
| 24 | Ceshui | LSJ04 | 7.4 | 2.06 | 8.6 | 0.0640 |
| 25 | Ceshui | LSJ05 | 0.4 | 2.06 | 8.0 | 0.0110 |

Table 4. Comparison of the shale gas reservoir rocks in central Hunan with other worldwide shale gas source rocks. Setting = depositional environment of source rocks; TOC – Total Organic Carbon; Kerogen = Kerogen Type; Ro = Vitrinite reflectance values; GAC = Gas adsorbtion capacity. Data for Ceshui, Dalong and Longtan shales from this paper; sources for other data from the study by Dong et al.(2016).

| **Shale unit** | **Ceshui shale (China)** | **Dalong Shale (China)** | **Longtan Shale (China)** | **Wufeng-Longmaxi Shale(China)** | **Haynesville Shale (US)** | **Woodford shale (US)** | **Barnett Shale (US)** |
|---|---|---|---|---|---|---|---|
| Age | Carboniferous | Permian | Permian | Ordovician-Silurian | Jurassic | Devonian | Carboniferous |
| Setting | Transitional | Transitional | Transitional | Marine | Marine | Marine | Marine |
| TOC (%) | 0.4–9.0 ($\bar{x}$=2.3 ) | 0.4–6.6 ($\bar{x}$=3.2) | 0.8–9.2 ($\bar{x}$=5.2 ) | 0.4–25.7 ($\bar{x}$=2.6 ) | 3.0 | 5.3 | 3.7 |
| Kerogen | Ⅲ | Ⅱ | Ⅱ | Ⅰ－Ⅱ | Ⅰ－Ⅱ$_1$ | Ⅰ－Ⅱ$_1$ | Ⅱ$_1$ |
| Ro (%) | 1.8–2.8 ($\bar{x}$=1.8 ) | 1.1–1.8 ($\bar{x}$=1.4) | 1.1–1.9 ($\bar{x}$=1.5 ) | 1.6-3.6 | 1.5 | 1.5 | 1.6 |
| Brittle minerals (%) | 30.9–67.5 ($\bar{x}$=55.0 ) | 55.2–89.9 ($\bar{x}$=75.8 ) | 50.8–70.3 ($\bar{x}$=58.9) | 21.0-44.0 | 35.0-65.0 | 50.0-75.0 | 40.0-60.0 |
| Porosity (%) | 1.4-8.6 ($\bar{x}$=5.0 ) | 0.5-12.0 ($\bar{x}$=5.7 ) | 5.6-14.0 ($\bar{x}$=9.3 ) | 5.2 | 8.3 | 5.0 | 5.0 |
| Permeability (mD) | 0.003-0.064 ($\bar{x}$=0.018 ) | 0.003-0.047 ($\bar{x}$=0.011 ) | 0.003-0.025 ($\bar{x}$=0.011 ) | 0.221 | 0.350 | 0.050 | 0.050 |

# Figures

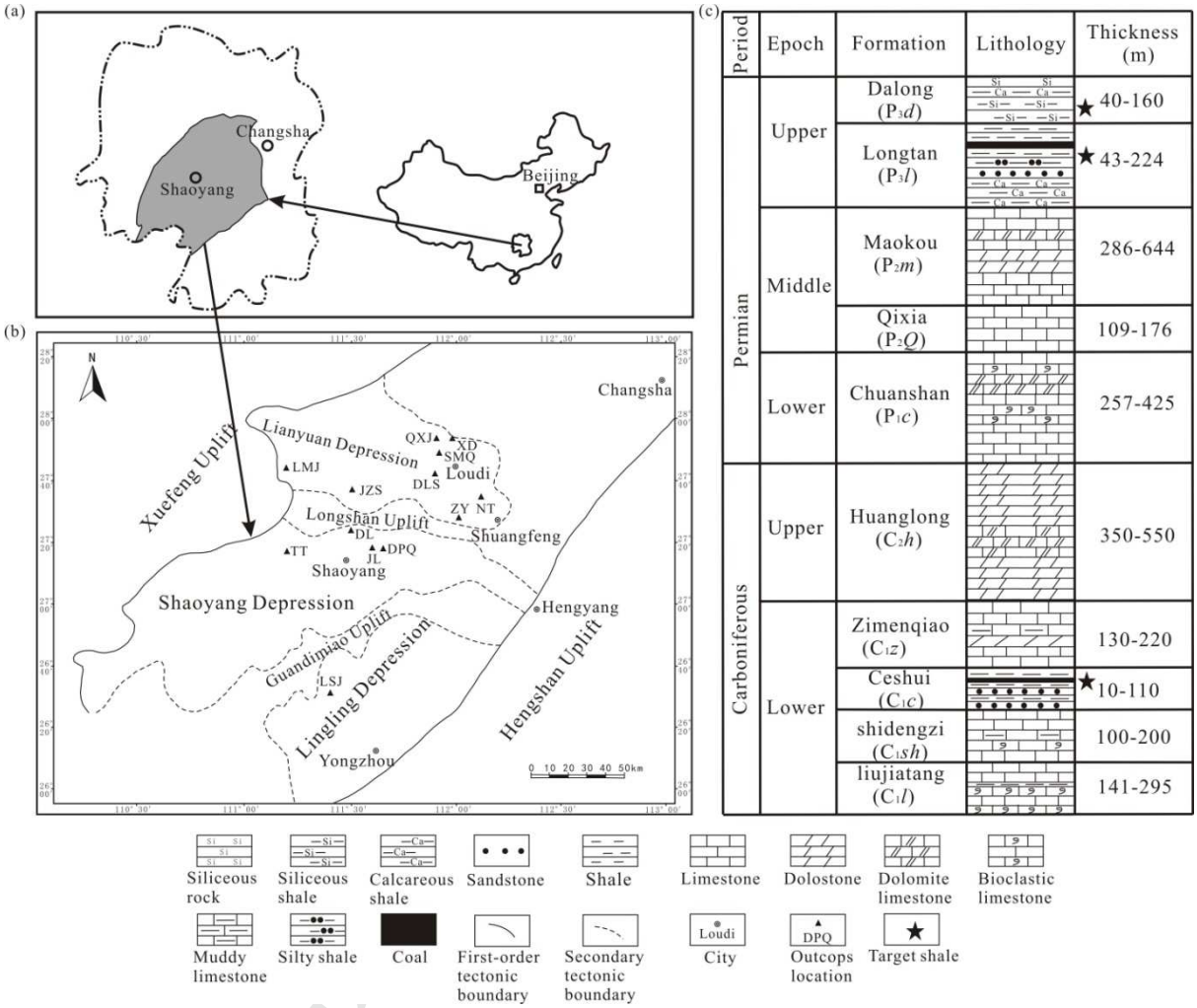


Figure1 (a) The position of Hunan Province and study area; (b) Regional geological map and sampling locations; (c) Generalized stratigraphic column of Permo-Carboniferous strata of the study area (Modified after Jing et al., 2013).

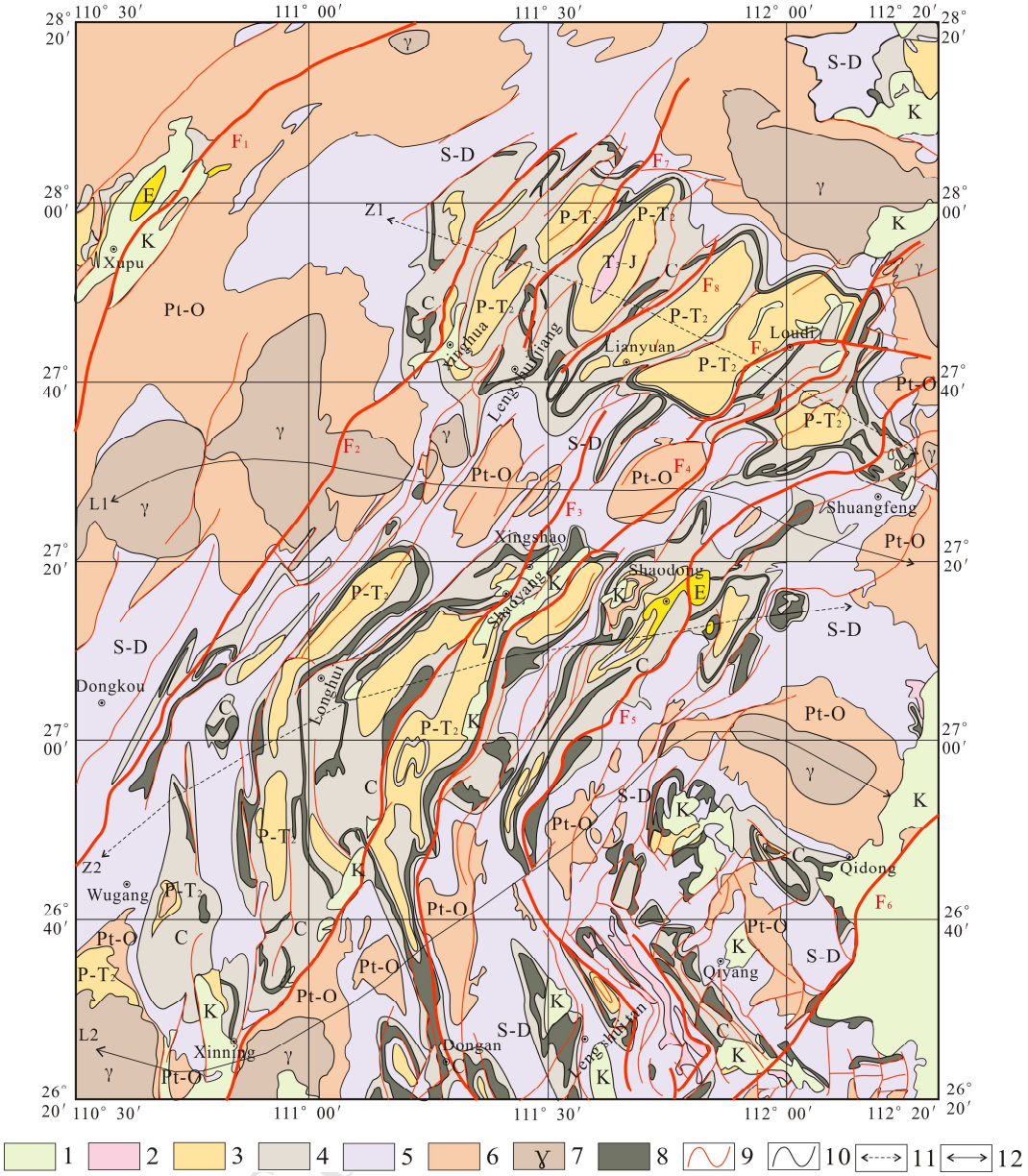


Figure 2 Structure geology map of the central Hunan (Modified from Li et al. 2013). 1. Cretaceous; 2. Upper Triassi-Jurassic; 3. Permian-Middle Triassic; 4. Carboniferous; 5. Silurian-Devonian; 6. Proterozoic-Ordovician; 7. Magmatic body; 8. Coal measures; 9. Fault line; 10. Stratigraphic boundary; 11. Depression; 12. Uplift; F1. Anhua-Xupu fault; F2. Chengbu-Xinhua fault; F3. Xinshao-Xinning fault; F4. Miluo-Shaoyang fault; F5. Qiyang Arc fault; F6. Zhuzhou-Shuangpai fault; F7. Jiyun fault; F8. Jinpanlun fault; F9. Fengguanshan fault; Z1. Lianyuan Depression; Z2. Shaoyang Depression; L1. Baimashan-Longshan bead-shape uplift; L2. Niuxingzhai-guandimiao bead-shape uplift.

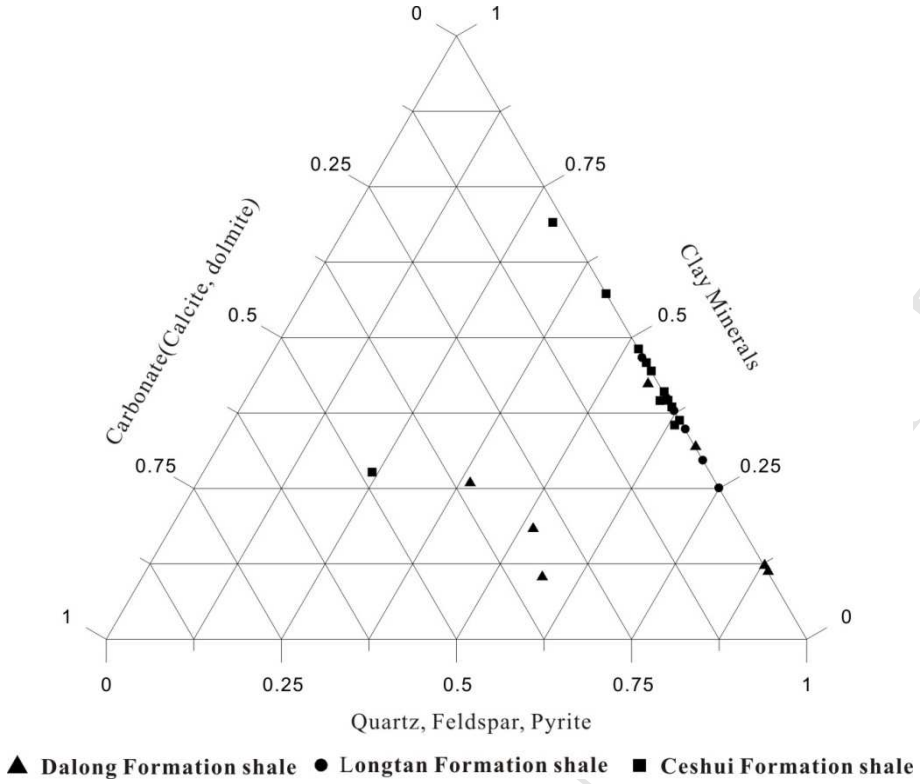


Figure 3. Ternary diagram of mineralogical constituents

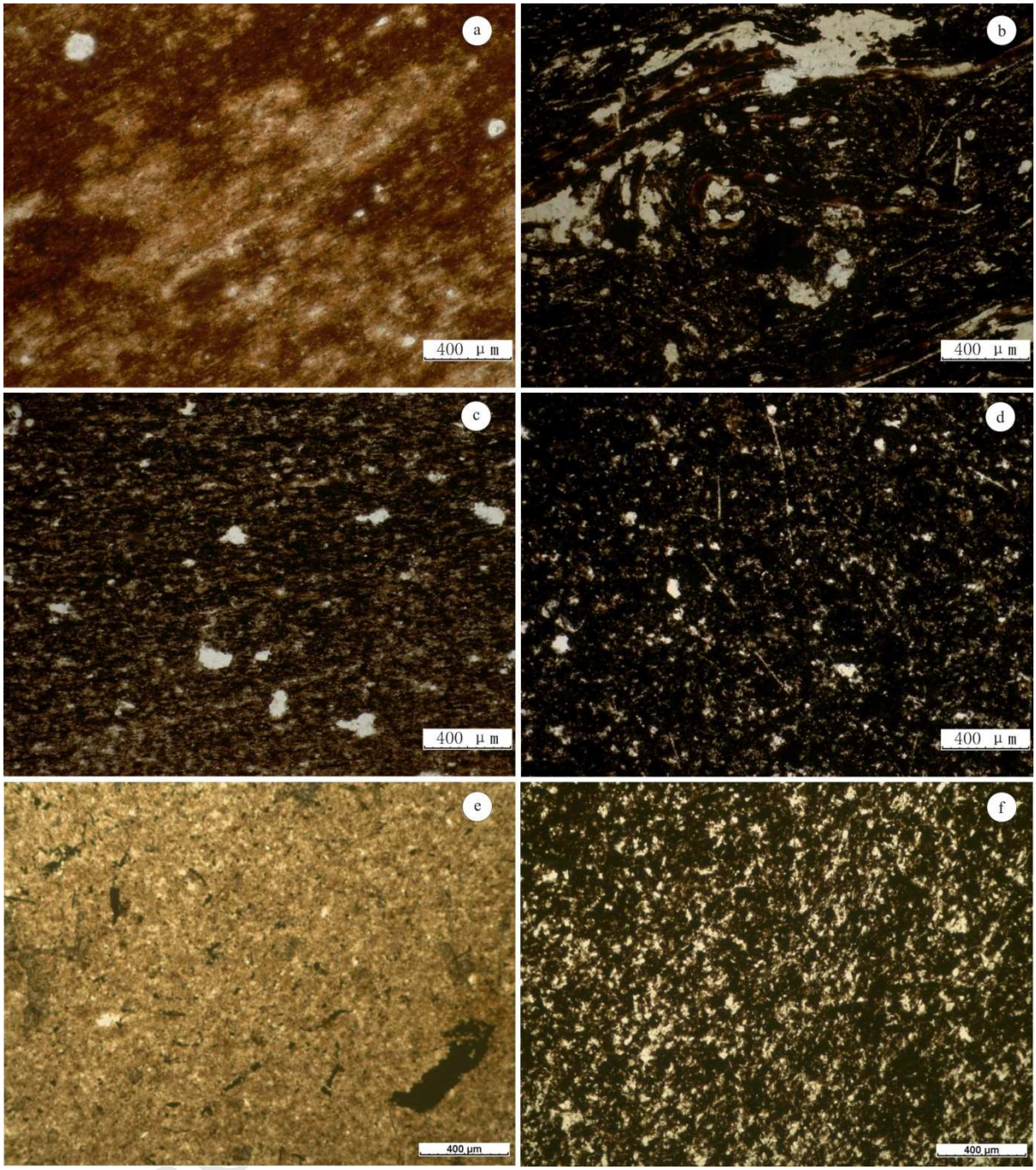


Figure 4. Micro-photographic images of Carboniferous-Permian shale samples. (a) Upper Permian Dalong calcareous shale (QXJ05) from the Qixingjie section. Quartz and carbonate concentrate in the white laminae, while clay and organic matter concentrate in the black laminae. (b) Upper Permian Dalong nonlaminated shale (DPQ06) from the Duanpoqiao section. The dark area is mainly composed of organic matter and clay, while the light area primarily comprises quartz and feldspar. (c) Upper Permian Longtan nonlaminated shale (NT02) from the Nantang section. The dark area consists of organic matter and clay, and the light is mainly quartz. (d) Upper Permian Longtan carbonaceous shale (DLS05) from the Doulishan section. The dark area is mainly organic matter and clay, and the light is mainly quartz and feldspar. (e) Lower Carboniferous Ceshui silty shale (LMJ06) from the

Lumaojiang section. Clay minerals occupy a large area in the texture, while organic matter and quartz scatter in the matrix. (f) Lower Carboniferous Ceshui carbonaceous shale (LSJ04) from the Liangshuijing section. The dark place is mainly organic matter and the light is mainly quartz. Organic matter aggregates or particles are randomly distributed in the matrix.

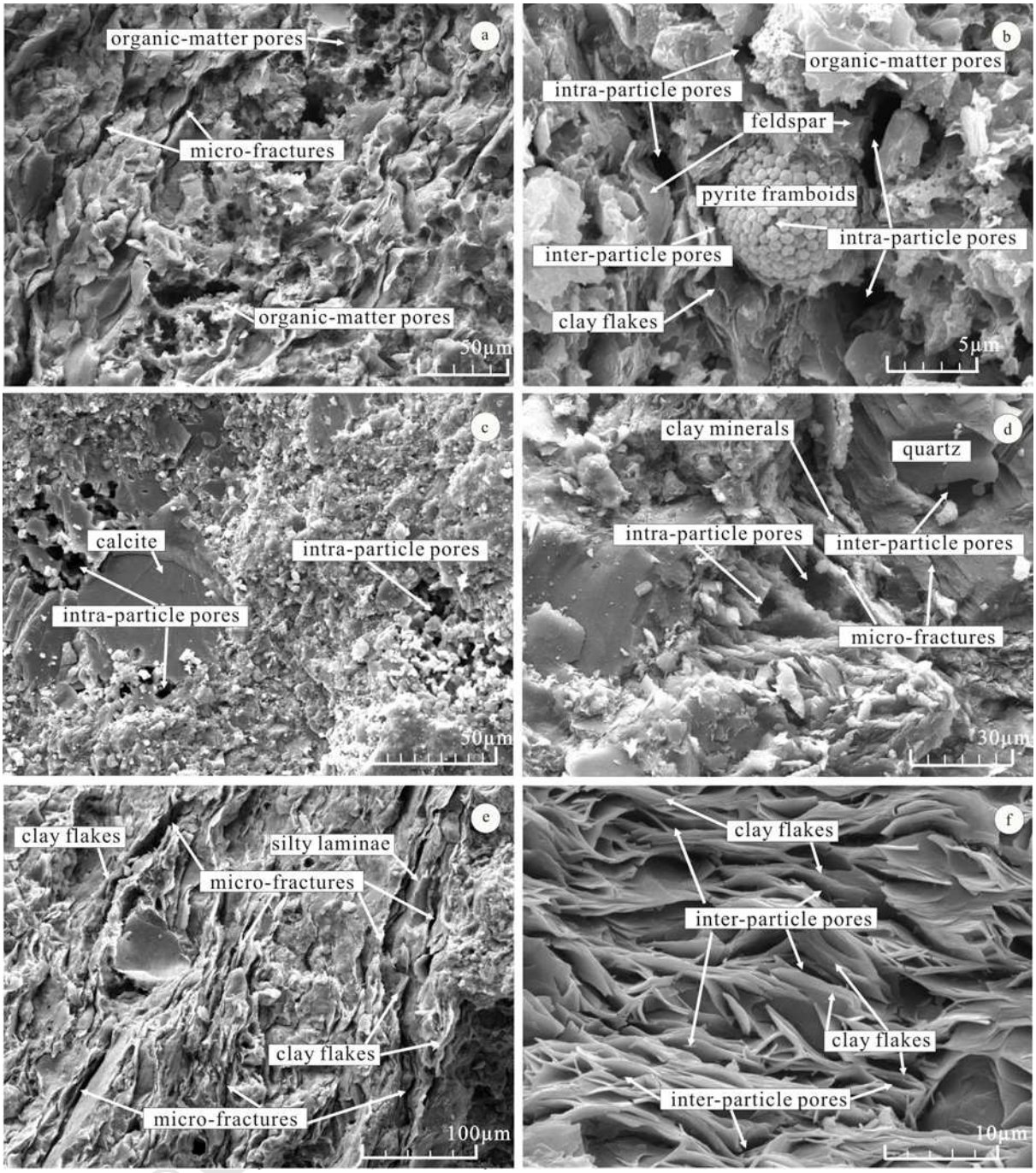


Figure 5. SEM images of Carboniferous–Permian shale samples. (a) Lower Carboniferous Ceshui carbonaceous shale (LSJ04) from the Liangshuijing section. “Honeycomb” organic pores and miro-fractures are well developed. (b) Upper Permian Longtan carbonaceous shale (DLS05) from the Doulishan section. Intra-particle pores exist in the pyrite framboids and the feldspar minerals. Inter–particle pores between pyrite crystals and clay flakes, and “honeycomb” organic–matter pores generated by hydrocarbon expulsion are well developed. (c) Upper Permian Dalong calcareous shale (QXJ02) from the Qixingjie section. Intra-particle pores in the carbonate minerals are well developed. (d) Upper Permian Dalong shale (DPQ03) from the Duanpoqiao section. Inter–particle pores occur between quartz minerals, intra–particle pores exist in the feldspar minerals and miro-fractures in clay

minerals and at weak interfaces are well developed. (e) Lower Carboniferous Ceshui carbonaceous shale (LSJ05) from the Liangshuijing section. Micro-fractures between clay flakes or between clay laminae and silty laminae are well developed. (f) Lower Carboniferous Ceshui silty shale (LMJ06) from the Lumaojiang section. Inter-particle pores in the clay flakes are well developed.

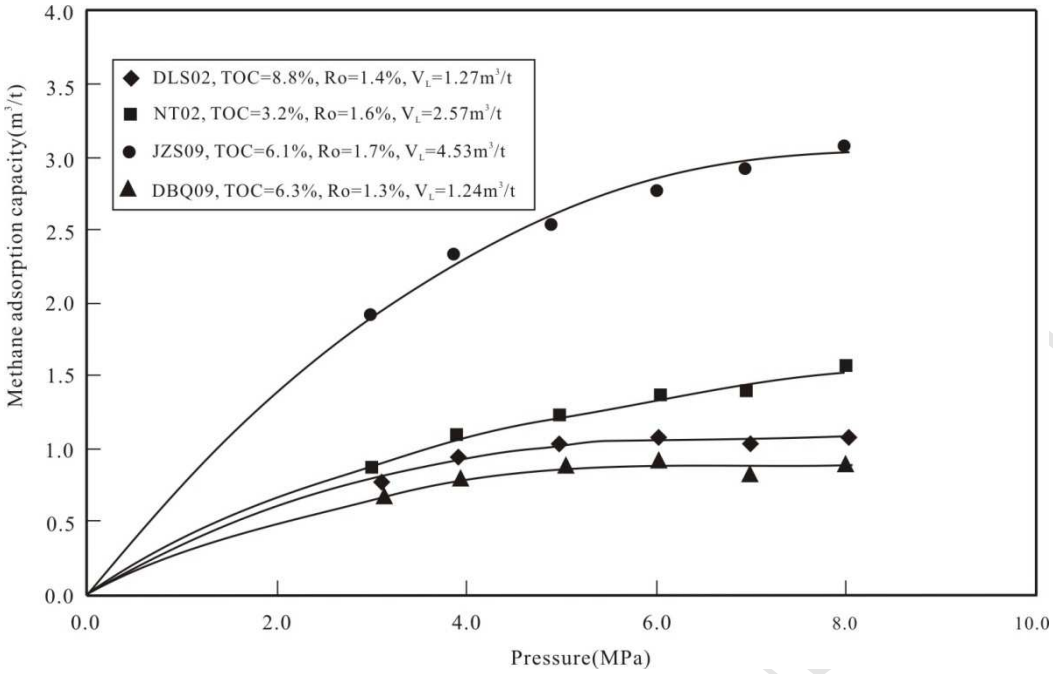


Figure 6. Methane adsorption isotherms at 40 °C

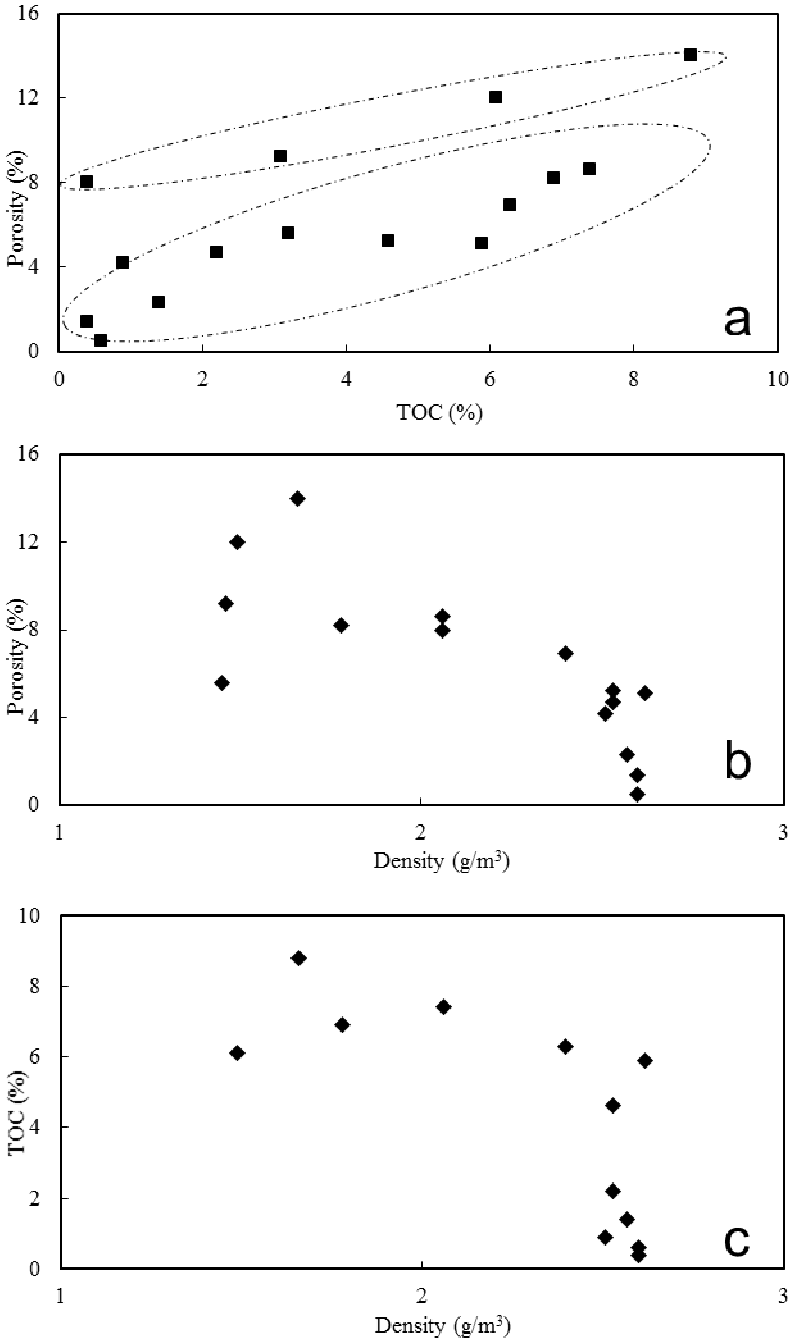


Figure 7. Correlation plots of porosity with (a) TOC content, (b) density, and (c) TOC content with density for Permo-Carboniferous shale samples in Central Hunan Province.

- Methane adsorption capacity is between 1.24 cm3/g and 4.53 cm3/g.
- Mean porosity and permeability are 6.4% and 0.013md, respectively.
- Carboniferous and Permian shales are abundant in type III and II organics, respectively.
- Thermal maturity is locating in the wet gas window.
- Mineral constituents are dominated by brittle minerals.